Chinese Chemical Letters 37 (2026) 111046

Contents lists available at ScienceDirect

Chinese Chemical Letters

journal homepage: www.elsevier.com/locate/cclet

Designing oxide-ion conductor in superstructural barium tellurate

Wei Wang[a,1], Guohong Cai[b,1], Guanqun Cai[c,*], Junliang Sun[b,*], Man-Rong Li[a,*]

[a] School of Chemistry and Chemical Engineering, Hainan University, Haikou 570228, China
[b] College of Chemistry and Molecular Engineering, Beijing National Laboratory for Molecular Sciences, Peking University, Beijing 100871, China
[c] Institute of Atomic and Molecular Physics, Sichuan University, Chengdu 610065, China

ARTICLE INFO

Article history:
Received 22 January 2025
Revised 26 February 2025
Accepted 5 March 2025
Available online 7 March 2025

Keywords:
Oxide-ion conductor
Electron diffraction
Superstructure
Oxide defect
Ion-migration mechanism

ABSTRACT

Searching for new oxide-ion conductors is of great significance in energy-related technologies. Here we identified a novel barium tellurate, $Ba_{10.55}Te_{4.45}O_{23.90}$, by chemical screening for superstructural oxide-ion conductors. Its crystal structure, solved from polycrystalline specimen by the combination of three-dimension electron diffraction, X-ray diffraction, and neutron diffraction, adopts a quadruple ($4 \times 4 \times 4$) cubic superstructure (*Fm*-3*m*, $a = 17.30612(2)$ Å) and can be regarded as a derivative of ABO_3 perovskite like $(Ba_{1.75}\square_{0.25})^{A}Ba^{B}W^{B'}O_{5.75}\square_{0.25}$. The ordered *A*-site metal vacancies and disordered oxygen vacancies are responsible for the enlarged superstructure. The titled compound is indeed an oxide-ion conductor but shows rather low ionic conductivity, owing to the high inter-polyhedral energy barrier of ionic migration. The discoveries unveil a new structural type for oxide-ion conductor exploration, and will evoke performance improvement by chemical modification such as aliovalent substitution.

© 2026 Published by Elsevier B.V. on behalf of Chinese Chemical Society and Institute of Materia Medica, Chinese Academy of Medical Sciences.

Oxide-ion conductors are of significant importance for energy related technologies [1,2], such as solid oxide fuel cells (SOFCs) [3–7], oxygen separation pumps and sensors [8], and solid oxide electrolysis cells (SOECs) [6]. The charge carrier in these materials is mostly oxygen vacancies, as discovered in perovskites [9,10], borates [11], fluorites, and scheelites [12], or oxygen interstitials, such as melilites [13,14], apatites [15], and $La_2Mo_2O_9$-based systems [16,17], or a mixture of oxygen vacancies and interstitials as in exotic perovskites [18]. The electrical conductivity of these materials is mainly governed by the defected oxygen sublattice to enable proper ionic diffusion at high temperature. Nowadays, a long-standing drawback of oxide-ion conductors is the relatively poor ionic transport in commercial materials at intermediate temperature [3], thus, it is essential to understand the mechanism for oxide ion charge carrier creation and mobility at atomic scale. The commonly applied strategy is to generate oxygen deficiency by aliovalent substitution in open-framework structures. For examples, partial replacement of Zr^{4+}/Ce^{4+} by Y^{3+}/Gd^{3+} in ZrO_2/CeO_2 creates oxygen vacancies in the well-known YSZ ($Zr_{1-x}Y_xO_{2-\delta}$) and GDC ($Ce_{1-x}Gd_xO_{2-\delta}$) [1,8]; paired co-doping of Sr^{2+}-Mg^{2+} at the La^{3+}-Ga^{3+} sites induces oxygen vacancy in $LaGaO_3$ to form LSGM ($La_{0.9}Sr_{0.1}Ga_{0.8}Mg_{0.2}O_{3-\delta}$) [19]. In contrast to the oxygen-deficient fluorites and perovskites by lower valence doping, higher-valence doping can generate oxygen interstitials as exemplified in the apatite and melilite series, which hold open-framework structures and adaptable coordination environment from tetrahedron to trigonal bipyramid [13–15]. The La-enriched non-stoichiometric $La_{1+x}Sr_{1-x}Ga_3O_{7+\delta}$ melilite demonstrates excellent oxygen-interstitial conductivity of 0.02–0.1 S/cm over 600–900 °C. The incorporation of oxygen interstitial modifies local tetragonal GaO_4 to trigonal bipyramid GaO_5 [13]. In addition to the doping policy, other approaches, such as cationic geometrical size-mismatch, can induce metal-deficiency and accordingly oxygen defect under charge balance.

Previous studies on the cryolite-type $Ba_{11}W_4O_{23}$ (BWO) unveiled the first quadruple perovskite-related $4 \times 4 \times 4$ superstructure phase, which accommodates ordered *A*-site metal vacancies, disordered oxygen, and anionic vacancies, and can be written as $[(Ba_{1.75}\square_{0.25})^{A}Ba^{B}W^{B'}O_{5.75}\square_{0.25}]_4$ derived from ABO_3 perovskite [20]. The cubic (*Fd*-3*m*) BWO contains statistically distributed oxygen and anionic vacancies, with three disordered oxygen sites in occupancy varying between 0.204 and 0.408, rendering average $WO_{18/3}$ coordination, indicating promising oxide-ion conductivity. However, BWO is metastable and can only be retained by temperature-quenching to liquid nitrogen from 1100 °C, which hinders further exploration of its electrical conductivity. Thermal stability analyses on the quenched BWO indicated that, it decomposed above 400 °C and recovered back at 1100 °C upon heating; while at the cooling process, although the superstructural phase

* Corresponding authors.
E-mail addresses: guanqun_cai@scu.edu.cn (G. Cai), junliang.sun@pku.edu.cn (J. Sun), limanrong@hainanu.edu.cn (M.-R. Li).
[1] These authors contributed equally to this work..

https://doi.org/10.1016/j.cclet.2025.111046
1001-8417/© 2026 Published by Elsevier B.V. on behalf of Chinese Chemical Society and Institute of Materia Medica, Chinese Academy of Medical Sciences.

can be retained to ambient temperature, impurity peaks appeared below 900 °C. Fortunately, BWO can be stabilized *via* partial replacement of W by Ta in $Ba_{11}W_{4-x}Ta_xO_{23-x/2}$ ($x \leq 2$), which shows pure oxide-ion conductivity over a wide oxygen partial pressure range and proton conductivity under wet-air below 800 °C [21]. The best performance is observed for the $x = 0.5$ case, showing comparable conductivity to the commercial YSZ, GDC, and LSGM around 400 °C. The above discoveries suggest that, unlike conventional perovskite, the incorporation of relatively large cations into the perovskite *B*-site can drive considerable metal vacancies and oxygen disorder, encouraging further exploration for promising oxide-ion conductors. Moreover, accommodation of Sr in the *B*-site of $Sr_{6-2x}Nb_{2+2x}O_{11+3x}$ ($Sr_2(Sr,Nb)^BNb^{B'}O_{6-\delta}$) leaves oxygen vacancies in the original anionic sites and also drives some oxygen into interstitial sites, as reported in the first discovery of oxygen interstitials in double perovskite by neutron diffraction technique [18]. Thus, it is exciting and evokes researchers to synthesize new oxide-ion conductors *via* similar structural engineering, namely size-mismatched modification at the perovskite-related structures.

Chemically, $Sr_{11}Re_4O_{24}$-type compounds [22–26], such as $Ba_{11}Os_4O_{24}$ and $BaLa_{10}Ir_4O_{24}$, seems similar to BWO but adopt tetragonal superstructure ($I4_1/a$, $a = 2\sqrt{2}a_p$, $c = 4a_p$, where a_p symbols the cell dimension of simple perovskite). Their structural formula can be written as $(A_{7/8}\square_{1/8})_2A^BB^{B'}O_6$ with 1/8 *A*-site vacancy, in which the chemical valence variation of the *B*-site cations like $Os^{+6/+7}$ or $Ir^{+4/+5}$ should be largely responsible for the cubic-to-tetragonal distortion and absence of oxygen disordering/vacancies under charge balance. From the chemical and geometric point of view, Te^{6+} and W^{6+} possess comparable oxidation state and ionic size. Presumably, barium tellurate, saying $Ba_{11}Te(VI)_4O_{23}$ if exists, could be a promising oxide-ion conductor as BWO. However, our attempts to make BWO-type $Ba_{11}Te_4O_{23}$ was unsuccessful, and yielded a mixture of an uncertain superstructural phase and several barium tellurates [27]. Modification of the Ba-Te ratio finally resulted in a novel line phase in starting ratio of Ba/Te = 9.5/4 other than the expected Ba/Te = 11/4. In this work, we described the discovery of this nominal $Ba_{9.50}Te_4O_{21.50}$ oxide-ion conductor, and solved its crystal structure *via* the combination of different diffraction techniques on polycrystalline specimen. The local crystal structure, electrical conductivity, and theoretical simulation were also studied to understand the ionic migration mechanism.

Our attempts to prepare $Ba_{11}Te_4O_{23}$ were unsuccessful, and finally a single phase was obtained by varying the Ba/Te ratio from 2.75 to ~2.38. SEM-EDS and ICP-OES results of the as-made product (Fig. S1 in Supporting information) revealed an average Ba/Te ratio of 2.375 and 2.33(2), respectively, in line with the starting ingredient proportions. Considering the charge equilibrium, the nominal composition can be written as $Ba_{9.50}Te_4O_{21.50}$. Initial structural phase analysis of the superfine PXD data does not match any known compounds in Ba-Te-O system [27–40], and chemically unstrained screening does not find any satisfying isostructural analogs. Thus, an *ab initio* indexing of the PXD data was carried out in TOPAS software [41], which yielded a cubic cell ($a \sim 17.3$ Å, Table S1 in Supporting information) with possible space group of *F*23 (No. 196), *Fm*-3 (No. 202), *F*432 (No. 209), *F*-43*m* (No. 216), or *Fm*-3*m* (No. 225) under the same extinction conditions. Therefore, 3D reciprocal lattice was reconstructed using the cRED technique for a clear image. As shown in Fig. 1 and Fig. S2 (Supporting information), the 3D-ED data illustrate the face-centered cubic unit cell parameters of $Ba_{9.50}Te_4O_{21.50}$ of $a = b = c \sim 17.3$ Å and $\alpha = \beta = \gamma = 90°$. The cubic lattice was further refined as $a = 17.30612(2)$ Å through the PXD data. Based on the *hkl* file reduced from 3D-ED data, the crystal structure of this nominal $Ba_{9.50}Te_4O_{21.50}$ oxide was solved in a quadruple perovskite structure with *Fm*-3*m* space group. Extraction of the structure factors from PXD data was carried out using the model-biased Le Bail method [42] based on the 3D-ED results, and direct procedures were then performed to get improved model for further model-biased extraction. Rietveld refinements were performed until no improvement was achieved after sequential iterations. The PXD data almost fit well, and positions of metal and three oxygen atoms were identified. However, Te2 atom was isolated, indicating the existence of low occupancy oxygen around, which cannot be captured by PXD diffraction. In succession, combined Rietveld refinements of the PXD and NPD data were evolved and the fitness of NPD data was totally unacceptable. As expected, disordered O4 was revealed around Te2 from Fourier and difference Fourier synthesis of NPD profiles (Fig. S3 in Supporting information). During refinements, the metal positions were recognized based on the metal-oxygen bond distances; occupancies of Ba1 and Te4 were restrained to maintain the metal ratio according to SEM-EDS results, and soft chemical restraint in light of electro-neutrality was applied to refine the O4 occupancy. The refinement parameters were histogram scale factors, background, unit cell parameters, peak profile coefficients, extinction coefficient (PXD only), atomic coordinates, atomic displacement parameters (ADPs), and occupancies for Te4, Ba1, and O4. The final refined profile fits are shown in Figs. 2a and b. The final refinement results and crystallographic data were presented in Tables S1-S4 (Supporting information).

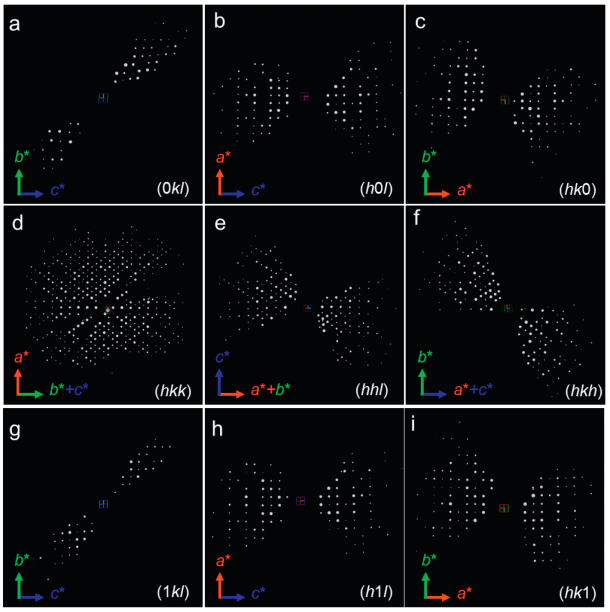


Fig. 1. 3D ED data of $Ba_{10.55}Te_{4.45}O_{23.90}$. The diffraction patterns of (a) (0*kl*), (b) (*h*0*l*), (c) (*hk*0), (d) (*hkk*), (e) (*hhl*), (f) (*hkh*), (g) (1*kl*), (h) (*h*1*l*) and (i) (*hk*1) slices extracted from the reconstructed 3D reciprocal lattice. The reflection conditions are: *hkl*: $h + k$, $h + l$, $k + l = 2n$; 0*kl*: k, $l = 2n$; *h*0*l*: h, $l = 2n$; *hk*0: h, $k = 2n$; *hkk*: $h + k = 2n$; *hhl*:$h + l = 2n$; *hkh*: $h + k = 2n$.

The Ba/Te ratio from combined PXD and NPD refinements converges to 2.371(1) and gives $Ba_{10.55}Te_{4.45}O_{23.90}$, which is in great agreement with the EDS result of 2.375. Original refinements with O2 and O3 at the 96*j* (y, z, 0) and 48*g* (1/4, 1/4, x) site, respectively, yielded unreasonably large atomic displacement parameters (ADPs) of O2 and O3, and too small ADPs for Te1. A close examination of the differential Fourier map based on the NPD data unveils somewhat density diffusion at O2 and O3 sites, indicating local site displacement. Therefore, each of them is set at a more general position with reduced occupancy. Decent results were obtained by placing O2 and O3 at doubled 192*l* (x, y, z) and 96*k* (x, x, z) site, respectively, with half occupancy as shown in Table S2. The threefold symmetry axis leads to the splitting of the O4 atom at 96*k* site into three. Soft restraint of the occupancy refinement for O4

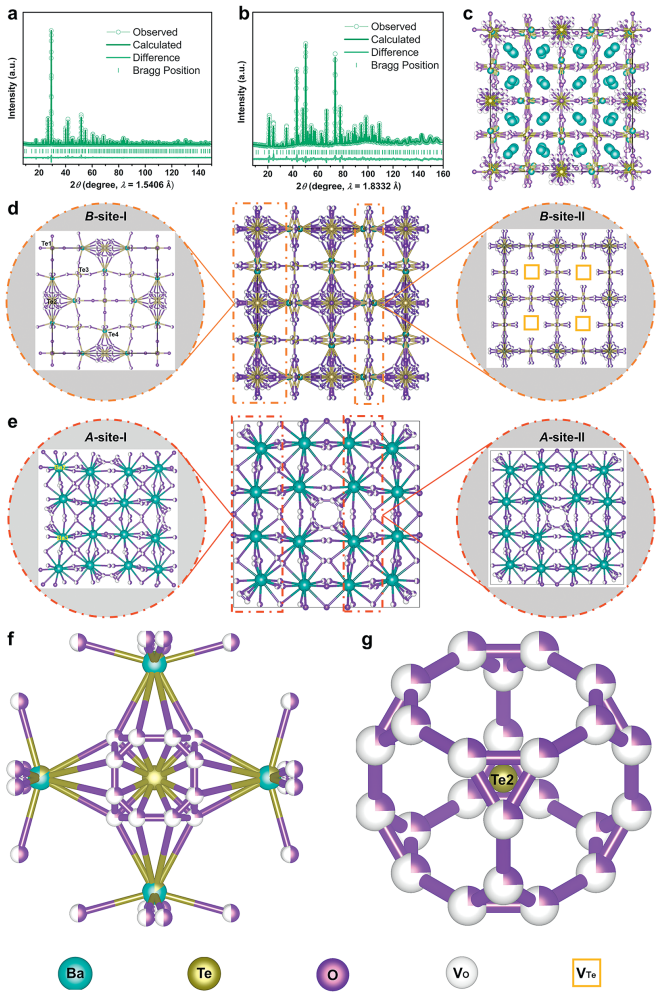


Fig. 2. Rietveld refinements and crystal structure of $Ba_{10.55}Te_{4.45}O_{23.90}$. The plots of (a) PXD and (b) NPD from joint refinements. (c) Perspective view of quadruple perovskite superstructure. (d) Crystal structure of the *B*-site sublattice in two different slabs, the left slab (*B*-site-I) is comprised of $Te1O_6$ and the average $Te2O_6$, $Te3O_6$, and $(Te4/Ba1)O_6$, the right slab (*B*-site-II) contains the average $Te3O_6$, $(Te4/Ba1)O_6$. (e) Crystal structure of the *A*-site sublattice in two different slabs comprised of Ba2-O and Ba3-O polyhedra. Local defect structure (f) face-sharing $Te2(O4)_{24\times0.242}$ and $(Te4/Ba1)(O2)_{8\times0.542}(O4)_{8\times0.242}$. (g) $(O4)_{24}$ cage around Te2 viewed along the C_3 direction in $Ba_{10.55}Te_{4.45}O_{23.90}$. The colorful atomic spheres and vacancy (V) squares are labeled on the bottom.

at (z, x, x) yielded 0.247(1), which is close to the expected value of 0.242 under charge balance giving Ba^{2+} and Te^{6+}. The refined crystal structure of the titled compound comprises 3 crystallographically independent Te sites, 2 Ba sites, 1 mixed Ba/Te site, and 4 oxygen sites (Table S2 and Fig. 2c). For a better visualization of the atomic arrangement, separated sections for the perovskite-related *A*- and *B*-sites in the structure were extracted (Figs. 2d and e). Unlike the *A*-site defected crystal structure of BWO [20,21], all *A* sites are filled by Ba atoms (Fig. 2e), while only 7/8 of *B* sites accommodate Te/Ba or Te atoms in $Ba_{10.55}Te_{4.45}O_{23.90}$. Approximately 1/8 *B*-site vacancies exist at the 8*c* (1/4, 1/4, 1/4) site (Fig. 2d, right). Consequently, the structure of $Ba_{10.55}Te_{4.45}O_{23.90}$ can be regarded as a $4\times4\times4$ supercell perovskite $(ABO_3)_4$ due to the positional order of Te, Ba/Te mixing, and cationic and anionic vacancies. According to the aforementioned analyses, the structural formula of $Ba_{10.55}Te_{4.45}O_{23.90}$ with *B*-site and anionic vacancies can be written in quadruple-perovskite style $Ba_4(Ba_{1.28}Te_{2.22}\square_{0.50})O_{11.94}\square_{0.06}$, namely $(ABO_3)_4$ in $[(Ba)^A(Ba_{0.320}Te_{0.555}\square_{0.125})^BO_{2.985}\square_{0.015}]_4$, where $\square$ symbols the vacancy. Notably, the Te/Ba mixing disrupts its local coordination environment from the octahedron. The Te/Ba atom at 24*e* site is surrounded by eight partially occupied O4, eight O2, and one O1 atom, forming a nearly statistical BO_6 coordination (Fig. 2f). Likewise, the Te2 at 4*b* site, caged by 24 partially occupied O4 atoms (Fig. 2g), suggest its average coordination number ~6. Te3 at 24*d* position is connected to eight O2 and four O3 atoms with half occupancy, also yielding nominal $Te3O_6$ octahedral environment. The above distinctive coordination polyhedron indicates the orientational disorder of the TeO_6 octahedra (Table S3). The oxygen defect in the nominal $Ba_{10.55}Te_{4.45}O_{23.90}$ suggests potential oxide ion conductivity as reported in other analogs.

In situ high-temperature PXD measurements were conducted to evaluate the thermal stability of the titled compound before any reliable temperature-dependent electrical conductivity evaluation. As shown in Fig. S4 (Supporting information), the phase evolution of $Ba_{10.55}Te_{4.45}O_{23.90}$ behaved differently upon heating and cooling. In Fig. S4a, upon heating, the supercell cubic phase was stable up to 700 °C and transformed into Ba_3TeO_6 and small amount of other barium tellurates. Then, the pure cubic superstructural phase was recovered above 950 °C. The precise recovering temperature must be around 950 °C and was not determined in this investigation. Stepwise cooling (Fig. S4b) resulted in almost no change, and the cubic phase was retained to room temperature. Here the overall trend of thermal stability of $Ba_{10.55}Te_{4.45}O_{23.90}$ upon heating and cooling is similar to that of BWO [20], the difference is that, BWO is partially decomposed upon programmable cooling and can only be retained by temperature quenching, while $Ba_{10.55}Te_{4.45}O_{23.90}$ is stable during the experimentally programmable cooling. More work is being undertaken to characterize the intermediate and slow cooled phases that will not be discussed in this paper. Apparently, the thermodynamic stability trend of $Ba_{10.55}Te_{4.45}O_{23.90}$ is not equivalent at experimental condition, and the temperature dependent electrical conductivity measurements should be carried out upon cooling.

Thereby, the total electrical conductivity of $Ba_{10.55}Te_{4.45}O_{23.90}$ was firstly measured on a sintered bar-pellet with relative density

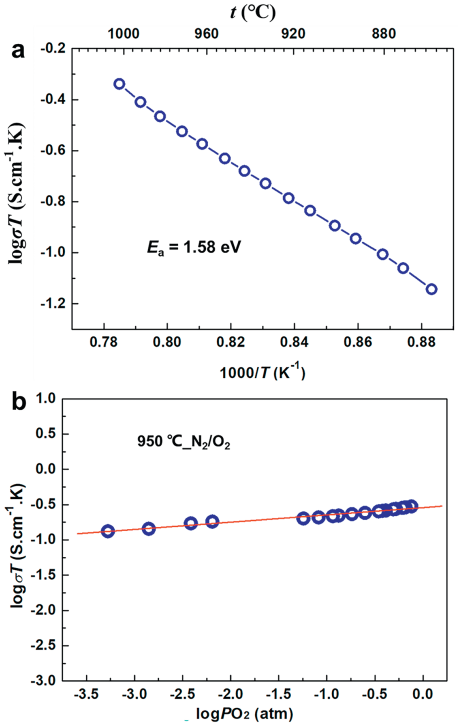


Fig. 3. Electrical conductivity of $Ba_{10.55}Te_{4.45}O_{23.90}$. (a) Arrhenius plot showing the temperature dependence of electrical conductivity under air; (b) Oxygen partial pressure (PO_2) dependent electrical conductivity at 950 °C under O_2-N_2 pair.

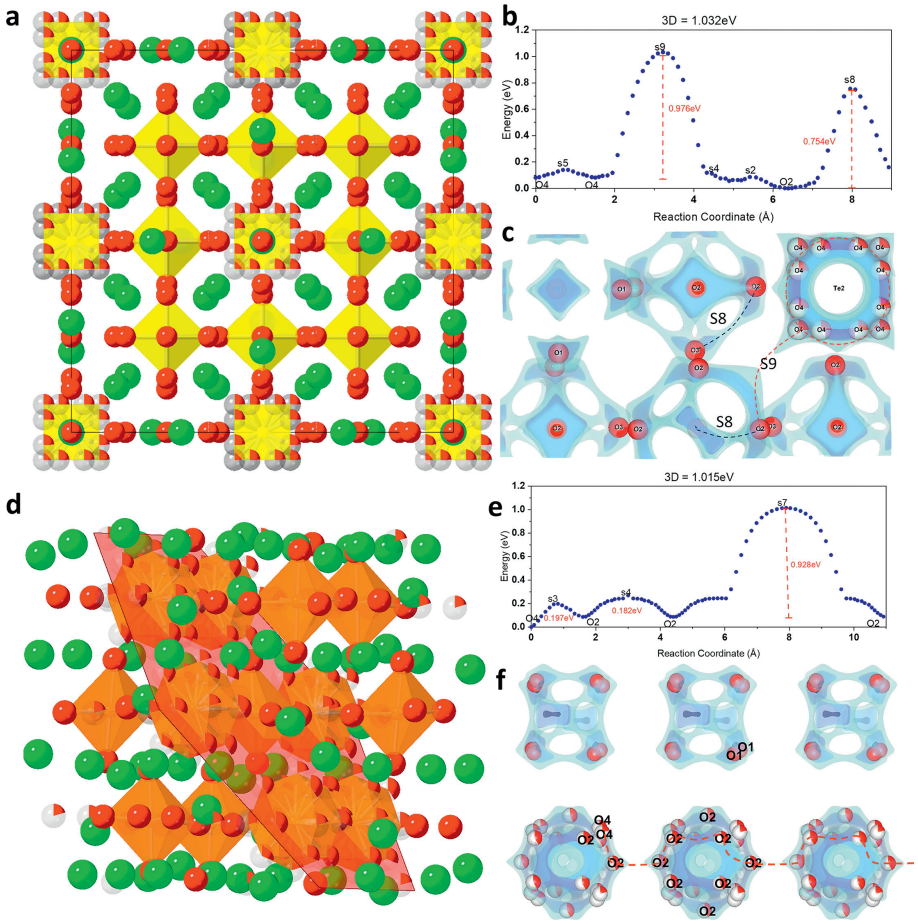


Fig. 4. BVSE theoretical analysis. (a) The average crystal structure of $Ba_{10.55}Te_{4.45}O_{23.90}$; Ba, green spheres; O, red spheres; anionic vacancy, white spheres; TeO_6 polyhedra, yellow. (b) Calculated BVSE models of migration energy barriers for $Ba_{10.55}Te_{4.45}O_{23.90}$. (c) Calculated BVSE isosurface map for $Ba_{10.55}Te_{4.45}O_{23.90}$, here the dashed lines highlight the calculated migration path. (d) The average crystal structure of $Ba_{11}W_4O_{23}$; Ba, green spheres; O, red spheres; anionic vacancy, white spheres; WO_6 polyhedra, orange-red. (e) Calculated BVSE models of migration energy barriers for $Ba_{11}W_4O_{23}$. (f) Calculated BVSE isosurface map for $Ba_{11}W_4O_{23}$. The dashed lines highlight the calculated migration path.

~83 % by four probe d.c. method in air, upon cooling in light of *in situ* high temperature PXD results. For the temperature range studied, the conductivity increases from 1.47×10^{-5} S/cm (850 °C) to 6.60×10^{-4} S/cm (1000 °C) with calculated activation energy of 1.58 eV ($\log\sigma T$ based, Fig. 3a), which is somewhat too high compared with the Ta-doped BWO (0.78 eV) [21] and other conventional conductors (0.7–1.0 eV), such as YSZ ($Y_{0.148}Zr_{0.852}O_{1.926}$) [8] and LSGM ($La_{0.9}Sr_{0.1}Ga_{0.8}Mg_{0.2}O_{3-\delta}$) [1,6]. Fig. 3b shows the plot of $\log(\sigma T/S\ \mathrm{cm^{-1}\,K})$ *versus* $\log(P_{O_2}/\mathrm{atm})$ at 950 °C under N_2/O_2 gas pair for $Ba_{10.55}Te_{4.45}O_{23.90}$. The conductivity appears to increase with increasing P_{O_2} in the range of $-4 \le \log(P_{O_2}) \le 0$, the rate($|\partial \log\sigma / \partial \log P_{O_2}|$) is about 1/10 ($0 < 1/10 < ¼$). We may thus, conclude that the present conductivity is a mixture of dominated ionic conduction with some *p*-type ingredient. In contrast, the conductivities under further reducing atmospheres could not be measured reproducibly because the conductivity values fluctuated (Fig. S4). Although the crystal structure of $Ba_{10.55}Te_{4.45}O_{23.90}$ contains considerable oxygen defect as in the BWO analogs, its electrical conductivity is rather poor. Thus, theoretical analysis was conducted to further understand the ionic migration path and energy barrier.

The BVSE method has been successfully applied to illustrate the ion migration process [43,44]. Based on the bond-valence sum (BVS) theory plus a morse-type potential, we calculated the entire energy landscape across the periodic structure. The most possible migration path can be determined by analyzing the connecting local minima and the relative energy barriers for each pathway segment. This method is particularly helpful for oxide-ion conductors with complex occupational and displacive disorder, which is usually computational expensive and difficult to cope with in *ab initio* calculations.

The average crystal structure of $Ba_{10.55}Te_{4.45}O_{23.90}$ in Fig. 4a shows the occupational disorder is concentrated in the O4 sites, forming unusual defective Te-O cubes (Fig. 2g). This disorder creates a low oxygen migration barrier inside the Te-O cube as shown by the continuous stocky isosurface connection between O4 atoms in Fig. 4c, and a migration energy barrier as low as 0.058 eV in Fig. 4b. However, these disordered cubes are surrounded by oxygen fully localized and occupied Te-O octahedra (Fig. 4a). If an oxygen atom moves from the cube to the Te-O octahedral network, it has to overcome an energy barrier as high as 0.976 eV (to pass the saddle point s9 in Fig. 4c). The migration barrier for oxygen atoms to migrate within the Te-O octahedral network is 0.754 eV from BVSE calculation. The BVSE calculations suggest, although we introduced considerable oxygen vacancies through compositional design to a stable cubic superstructure, the uneven distribution of the oxygen occupational disorder within the material results in a moderate oxygen conductivity. This observation is further consolidated by another example BWO, with a similar composition (substituting W with Te) and superstructure [20,21].

As shown in Fig. 4d, the occupational disorder in BWO is also concentrated on an irregular W-O polyhedral. What's different from $Ba_{10.55}Te_{4.45}O_{24}$ is, the oxygen fully occupied W-O octahedra are surrounded by 6 occupational disordered W-O irregular polyhedral on the (111) plane. Although the oxygen migration energy barrier across polyhedra to polyhedra (0.928 eV, Fig. 4e) in BWO is similar with that for $Ba_{10.55}Te_{4.45}O_{23.90}$ (0.976 eV, Fig. 4b), the connected disordered polyhedra with occupational disorder is more likely for oxygen atoms to migrate along certain path. This configuration endows oxygen atoms to migrate along the continuous disordered W-O polyhedra as highlighted by the red dotted line in Fig. 4f. Hence, experimentally, the BWO analog has a higher oxide ion conduction than $Ba_{10.55}Te_{4.45}O_{23.90}$. Obviously, the oxygen-ion conduction not only depends on the concentration of the vacancies, *i.e*., occupational disorder, but also relies on a continuous distribution of occupational disorder to lower the interpolyheral energy barrier along the ionic migration pathway.

The identified $Ba_{10.55}Te_{4.45}O_{23.90}$ adopts a novel perovskite derived quadruple superstructure $(ABO_3)_4$ with ordered *B*-site vacancies and disordered oxygen vacancies in $[(Ba)^A(Ba_{0.320}Te_{0.555}\square_{0.125})^BO_{2.985}\square_{0.015}]_4$, as solved *via* the combination of electron, X-ray, and neutron diffraction techniques from the polycrystalline sample. The existence of oxygen vacancies is further evidenced by the electrical conductivity measurements, which indicate nearly pure oxide ion conductivity above 800 °C. Given the considerable oxygen vacancies, the oxide ion conductivity is rather poor compared with the parent superstructural materials and conventional oxide electrolytes. Theoretical simulation reveals that, although the energy barrier of intra-polyhedral oxide-ion migration is very small (0.058 eV), the value of inter-polyhedral oxide-ion migration is as high as 0.976 eV, which is responsible for the overall low electrical conductivity in $Ba_{10.55}Te_{4.45}O_{23.90}$. Nevertheless, the discovery of $Ba_{10.55}Te_{4.45}O_{23.90}$ proposes a new superstructure type to guide the design of new materials, and the physical properties like electrical conductivity, are expected to be significantly improved by chemical modification, such as chemical doping at the *B*-site by lower valence cations to increase oxygen vacancies at the neighbor polyhedron to reduce the energy barrier for oxide-on diffusion.

Declaration of competing interest

The authors declare that they have no known competing financial interests or personal relationships that could have appeared to influence the work reported in this paper.

CRediT authorship contribution statement

Wei Wang: Writing – review & editing, Writing – original draft, Investigation, Formal analysis, Conceptualization. **Guohong Cai:** Writing – review & editing, Writing – original draft, Investigation, Formal analysis. **Guanqun Cai:** Writing – review & editing, Writing – original draft, Formal analysis. **Junliang Sun:** Writing – review & editing, Supervision, Conceptualization. **Man-Rong Li:** Writing – review & editing, Writing – original draft, Supervision, Conceptualization.

Acknowledgments

This work was financially supported by the Hainan Provincial Natural Science Foundation of China (No. 524RC473), the National Science Foundation of China (NSFC, Nos. 22090041, 22125102, U21A20285 and 12350710177), the Program for Guangdong Introducing Innovative and Entrepreneurial Teams (No. 2017ZT07C069), and the Guangdong Basic and Applied Basic Research Foundation (No. 2022B1515120014). The authors would like to thank Dr. Seung-Tae Hong at Daegu Gyeongbuk Insitute of Science and Technology for helpful discussion.

Supplementary materials

Supplementary material associated with this article can be found, in the online version, at doi:10.1016/j.cclet.2025.111046.

References

[1] J.B. Goodenough, Annu. Rev. Mater. Res. 33 (2003) 91–128.
[2] J.H. Shim, Nat. Energy 3 (2018) 168–169.
[3] E.D. Wachsman, K.T. Lee, Science 334 (2011) 935–939.
[4] P. Boldrin, N.P. Brandon, Nat. Catal. 2 (2019) 571–577.
[5] Y. Lyu, J. Xie, D. Wang, J. Wang, J. Mater. Sci. 55 (2020) 7184–7207.
[6] S. Hussain, L. Yangping, Energy Trans. 4 (2020) 113–126.
[7] H. Bao, S.X. Leong, J.R.T. Chen, et al., CCS Chem. 6 (2024) 1403–1421.
[8] Y. Yang, Y. Zhang, M. Yan, Sep. Purif. Technol. 298 (2022) 121627.
[9] M. Li, M.J. Pietrowski, R.A. De Souza, et al., Nat. Mater. 13 (2014) 31–35.
[10] F. Jie, Z. Lei, Z. Wenda, et al., Chin. Chem. Lett. 34 (2023) 107551.
[11] X. Li, L. Yang, Z. Zhu, et al., Sci. China Mater. 65 (2022) 2737–2745.
[12] X. Yang, A.J. Fernández-Carrión, J. Wang, et al., Nat. Commun. 9 (2018) 4484.
[13] X. Kuang, M.A. Green, H. Niu, et al., Nat. Mater. 7 (2008) 498–504.
[14] M.R. Li, X. Kuang, S.Y. Chong, et al., Angew. Chem. Int Ed. 49 (2010) 2362–2366.
[15] E. Kendrick, J. Kendrick, K.S. Knight, et al., Nat. Mater. 6 (2007) 871–875.
[16] I.R. Evans, J.A.K. Howard, J.S.O. Evans, Chem. Mater. 17 (2005) 4074–4077.
[17] P. Lacorre, F. Goutenoire, O. Bohnke, et al., Nature 404 (2000) 856–858.
[18] M.R. Li, S.T. Hong, Chem. Mater. 20 (2008) 2736–2741.
[19] K. Huang, J.H. Wan, J.B. Goodenough, J. Electrochem. Soc. 148 (2001) A788.
[20] S.T. Hong, J. Solid State Chem. 180 (2007) 3039–3048.
[21] J.S. Ha, E. Lee, S.T. Hong, H.I. Yoo, Solid. State. Commun. 179 (2008) 1066–1070.
[22] K.G. Bramnik, G. Miehe, H. Ehrenberg, et al., J. Solid. State. Chem. 149 (2000) 49–55.
[23] M. Wakeshima, Y. Hinatsu, Solid. State. Commun. 136 (2005) 499–503.
[24] W. Jeitschko, H.A. Mons, U.C. Rodewald, et al., Z. Naturforsch. B 53 (1998) 31–36.
[25] Q. Zhao, F. Han, C.C. Stoumpos, et al., Sci. Rep. 5 (2015) 11705.
[26] T. Ferreira, M.D. Smith, H.C. zur Loye, Inorg. Chem. 57 (2018) 7797–7804.
[27] D.K. Kwon, M.T. Lanagan, T.R. Shrout, Mater. Lett. 61 (2007) 1827–1831.
[28] M.G. Johnston, W.T.A. Harrison, J. Am. Chem. Soc. 124 (2002) 4576–4577.
[29] D.K. Kwon, M.T. Lanagan, T.R. Shrout, J. Am. Ceram. Soc. 88 (2005) 3419–3422.
[30] D. Hamani, A. Plat, M. Colas, et al., J. Alloys. Compd. 661 (2016) 92–99.
[31] K.K. Mishra, S.N. Achary, S. Chandra, et al., Inorg. Chem. 55 (2016) 227–238.
[32] D. Hottentot, B.O. Loopstra, Acta Crystallogr. Sect. C 39 (1983) 320–322.
[33] S. Natansohn, J. Electrochem. Soc. 120 (1973) 660.
[34] P.M. Almond, M.L. McKee, T.E. Albrecht-Schmitt, Angew. Chem. Int. Ed. 41 (2002) 3426–3429.
[35] K.K. Mishra, S.N. Achary, S. Chandra, et al., Inorg. Chem. 55 (2016) 8994–9005.
[36] F. Folger, Z. fur. Anorg. Allg. Chem. 411 (1975) 111–117.
[37] B. Stöger, M. Weil, E. Zobetz, Z. Kristallog. 225 (2010) 125–138.
[38] M. Koçak, C. Platte, M. Trömel, Z. Anorg. Allg. Chem. 453 (1979) 93–97.
[39] I. Grelowska, M. Reben, B. Burtan, et al., J. Mol. Struct. 1126 (2016) 219–225.
[40] M. Kocak, C. Platte, M. Tromel, Acta Crystallogr. Sect. B 35 (1979) 1439–1441.
[41] L.L. Wong, K.C. Phuah, R. Dai, Chem. Mater. 33 (2021) 625–641.
[42] A. Le Bail, Powder Diffr. 20 (2005) 316–326.
[43] S. Fop, K. McCombie, R.I. Smith, Chem. Mater. 32 (2020) 4724–4733.
[44] N.A. Kabanova, Y.A. Morkhova, A.V. Antonyuk, et al., Solid State Ion. 391 (2023) 116142.